Solar-Blind Avalanche Photodetector Based On Single ZnO–Ga$_2$O$_3$ Core–Shell Microwire

Bin Zhao,[†,‡] Fei Wang,[†] Hongyu Chen,[§] Yunpeng Wang,[†] Mingming Jiang,[†] Xiaosheng Fang,*[,§] and Dongxu Zhao*[,†]

[†]State Key Laboratory of Luminescence and Applications, Changchun Institute of Optics, Fine Mechanics and Physics, Chinese Academy of Sciences, No. 3888 Dongnanhu Road, Changchun 130033, People's Republic of China

[‡]Graduate University of the Chinese Academy of Sciences, Beijing 100049, People's Republic of China

[§]Department of Materials Science, Fudan University, Shanghai 200433, People's Republic of China

S *Supporting Information*

ABSTRACT: High-performance solar-blind (200–280 nm) avalanche photodetectors (APDs) were fabricated based on highly crystallized ZnO–Ga$_2$O$_3$ core–shell microwires. The responsivity can reach up to 1.3×10^3 A/W under −6 V bias. Moreover, the corresponding detectivity was as high as 9.91×10^{14} cm·Hz$^{1/2}$/W. The device also showed a fast response, with a rise time shorter than 20 μs and a decay time of 42 μs. The quality of the detectors in solar-blind waveband is comparable to or even higher than that of commercial Si APD (APD120A2 from Thorlabs Inc.), with a responsivity ~8 A/W, detectivity ~10^{12} cm·Hz$^{1/2}$/W, and response time ~20 ns. The high performance of this APD make it highly suitable for practical applications as solar-blind photodetectors, and this core–shell microstructure heterojunction design method would provide a new approach for realizing an APD device.

KEYWORDS: core–shell microwires, solar-blind photodetectors, avalanche photodectors
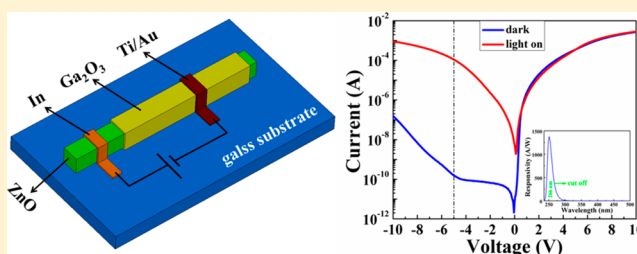
Solar-blind (200–280 nm) photodetectors, which utilize the "black background" on Earth, have found a vast and ever growing number of applications, including missile warning, fire alarms, short-range communication security, environmental studies, chemical/biological analysis, and ultraviolet (UV) astronomy.[1−7] Because the solar-blind signals are generally weak, more attention has been paid to photodetectors with highly internal gain, such as nanostructures photodetectors with photoconductive gain or avalanche photodetectors (APDs) with avalanche gain.[8−11] Because the ideal photodetector should satisfy the 5S requirements, that is, high sensitivity, high signal-to-noise ratio, high spectral selectivity, high speed, and high stability,[4,12] the slow response time (~seconds) restricts the applications of nanostructures photodetectors for the persistent photoconductivity effect,[8,9] and APDs based on semiconductors are more appropriate alternatives. Unfortunately, the commercial APDs used in solar-blind detectors are primarily based on narrow-band semiconductor Si-based devices, that require expensive and cumbersome Woods optical filters.[2,13−15] A detector based on the wide band gap semiconductor Al$_x$Ga$_{1−x}$N alloy is a promising candidate, and the Al$_x$Ga$_{1−x}$N APDs have attracted substantial research interests.[16,17] However, it is difficult to produce highly crystallized Al$_x$Ga$_{1−x}$N thin films with high Al contents, which limits their application in solar-blind wavelengths detection.[2,18]

With a direct wide band gap (~4.9 eV), β-Ga$_2$O$_3$ is quite suitable for solar-blind photodetection.[18] Due to its single crystal structure, simple growth, and high responsivity,[18,19] more and more attention has been drawn on β-Ga$_2$O$_3$ nanostructure based photodetectors, such as nanowires, nanobelts, and nanosheets.[20−22] However, most of the detectors are of the photoconductive type, and the response is quite slow (~seconds), which does not satisfy the requirement of fast response. A photovoltaic detector with fast response would be the prefer choice, which is also the foundation in APD design.[23−25] Because β-Ga$_2$O$_3$ performs n-type rather than p-type conductivity, a heterojunction based on β-Ga$_2$O$_3$ is a feasible approach to fabricating a photovoltaic photodector.[26,27] The use of SiC and GaN film has been reported to in the fabrication of heterojunction solar-blind photodetector with β-Ga$_2$O$_3$, but the low crystal quality of the films weakens the performance of the device.[27,28]

Core–shell nanowires are highly suitable to design heterojunctions with high crystal quality;[29−32] they usually consist of low band gap cores and high band gap shells.[30,33,34] ZnO, which is easy to grow nanostructures and has a quite small lattice mismatch with Ga$_2$O$_3$, is appropriate for such

heterojunctions.[35−37] Moreover, the conduction-band offsets (ΔE_c) between ZnO and Ga_2O_3 is much larger than the valence-band offsets (ΔE_v), which could lead to the impact ionization of electrons to generate avalanche multiplication.[38−40] Parallel ZnO nanostructure shells have been grown on higher band gap Ga_2O_3 nanowire cores following a two-step approach to form Ga_2O_3−ZnO core−shell nanowires.[35,41] Unfortunately, a mass of defects in the grain boundary between the different materials led to the unsatisfactory electrical properties of those composite nanowires, thus diminishing their desirability as a photodetector.

In this Letter, ZnO−Ga_2O_3 core−shell microwires have been synthesized following a one-step approach, in which the ZnO core and the Ga_2O_3 shell were both single-crystalline, with hexagonal and monoclinic crystals, respectively. The ZnO crystal lattice could abruptly switch to the Ga_2O_3 crystal lattice within 6−8 atomic layers without incurring noticeable structure defects at the interface between the materials. A high performance solar-blind APD has been fabricated based on the ZnO−Ga_2O_3 core−shell microwire, and it demonstrated ultrahigh sensitivity, high signal-to-noise ratio, high spectral selectivity, high speed, and high stability. The high external quantum efficiency (EQE) of the device was confirmed to arise from the avalanche multiplication effect.

The scanning electronic microscopy (SEM) image of the core−shell microwire is shown in Figure 1a. The average
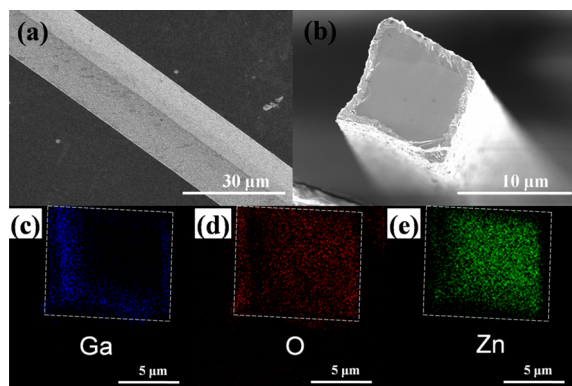

Figure 1. (a) SEM image of a Ga_2O_3−ZnO core−shell microwire. (b) Cross section SEM image demonstrates an obvious core−shell structure. The diameter of the core is approximately 9 μm and the thickness of the shell is approximately 500 nm. (c−e) The cross section EDS maps of Ga (c), O (d), and Zn (e), which demonstrates that Ga is mainly distributed in the outside shell layer, Zn is mainly distributed in the core, and O is distributed over the whole section.

diameter of the microwires is approximately 10 μm, and they have a length of 1−2 cm. Figure 1b shows the typical cross section SEM image of the microwire, unambiguously indicating that the microwire is a core−shell structure. The diameter of the core is approximately 9 μm and the thickness of the shell is approximately 500 nm. The cross-section distributions of the different elements, detected by energy dispersive spectroscopy (EDS) area scanning, are shown in Figure 1c−e. It can be observed that Ga is mainly distributed in the outside shell layer, Zn is mainly distributed in the core and O is distributed over the whole area, thus confirming that the prepared core−shell structure is a ZnO−Ga_2O_3 microwire. The glancing-angle-mode X-ray diffraction (XRD) pattern of the microwires is shown in Supporting Information Figure S1. According to the XRD analysis, the ZnO core is a hexagonal crystal system and

the Ga_2O_3 shell is a monoclinic crystal system corresponding to β-Ga_2O_3.

A low-magnification transmission electron microscopy (TEM) image of the cross-sectional slice of the microwire is shown in Figure 2a, from which we can clearly distinguish the
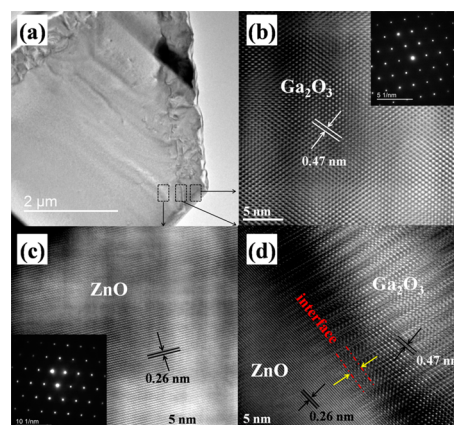

Figure 2. (a) Low-magnification TEM image of the cross sectional slice of the core−shell microwire. (b) HR-TEM image of the shell presenting a lattice spacing of 0.47 nm corresponding to ($\bar{2}$ 0 1) of monoclinic Ga_2O_3; the SAED pattern illustrated in the inset demonstrates the single-crystal structure. (c) HR-TEM image of the core showing a lattice spacing of 0.26 nm corresponding to (0 0 2) of hexagonal ZnO; the SAED pattern illustrated in the inset demonstrates the single-crystal structure. (d) HR-TEM image of the interface between the core and shell layers.

core from the shell. A high-resolution TEM (HR-TEM) image of the shell (shown in Figure 2b) demonstrates a lattice spacing of 0.47 nm that corresponds to the ($\bar{2}$ 0 1) plane separations of monoclinic β-Ga_2O_3. Moreover, the selected area electron diffraction (SAED) pattern illustrated in the inset of Figure 2b indicates that the shell presents a single-crystal structure. The HR-TEM image of the core (shown in Figure 2c) illustrates a lattice spacing of 0.26 nm that corresponds to the separation of the (0 0 2) planes of hexagonal ZnO, and the SAED pattern of the core confirms the single-crystal structure of the core ZnO. The HR-TEM image of the interface between the core and shell layers is shown in Figure 2d; it can be observed that the crystal lattices of the ZnO core and Ga_2O_3 shell show an abrupt transition in 6−8 atomic layers and that there are few noticeable structural defects at the interface between the materials.

The formation of the core−shell structure is due to the different growth temperature of ZnO (950 °C) and Ga_2O_3 (1100 °C) in a vapor−solid progress. The individual micro-structures of ZnO (microwire) and Ga_2O_3 (microbelt), synthesized at 1050 °C and at 1200 °C, respectively, are shown in Supporting Information Figure S2a and b. In the mixture powders in the one-step growth process, ZnO first reaches its growth temperature and then forms the microwire core. With the increasing temperature, the density of Zn vapor decreases; when the temperature reaches the growth temperature of Ga_2O_3, the Ga_2O_3 shell grows around the ZnO microwire core, thus forming the ZnO−Ga_2O_3 core−shell microwires.[42−44]

The schematic diagram of the ZnO−Ga_2O_3 core−shell microwire photodetector is shown in Figure 3a. The linear I−V curves of the ZnO microwire with In electrodes and the Ga_2O_3
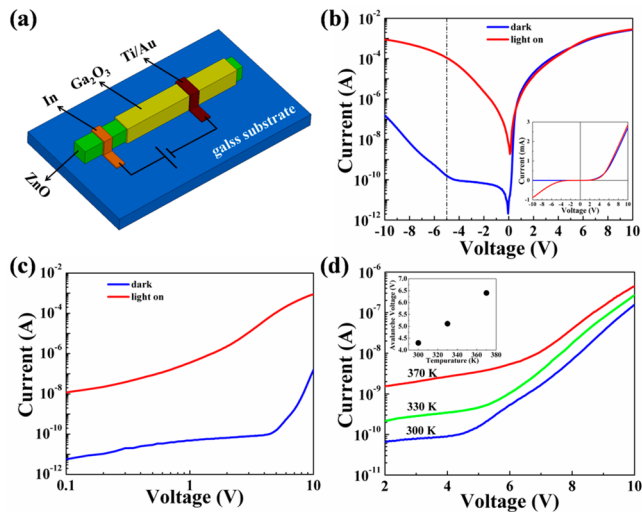
Figure 3. (a) Schematic diagram of the APD device. (b) The $I-V$ characteristics of the photodetector under dark and illumination with 254 nm light of 1.67 mW/cm^2. (c)The $I-V$ characteristics in the reverse bias shown in log−log coordinates. (d) $I-V$ characteristics at 300, 330, and 370 K in the reverse voltage under dark; the inset shows the dependence of the avalanche breakdown voltage on the recording temperature.

microbelt with Ti/Au electrodes are shown in Supporting Information Figure S3a and b and indicate the ohmic contacts. As shown by the blue line in Figure 3b, the $I-V$ curve of the device presents an off state in the reverse bias and an on state in the forward bias, which is a typical single junction rectifying property. The $I-V$ characteristic of the device under 254 nm light illumination with a power density of 1.67 mW/cm^2 is shown as a red line in Figure 3b. The photocurrents are $10^3 \sim 10^6$ times larger than the dark currents under the reverse biases. The device is a photovoltaic detector because the currents under the forward biases are little changed. To show the response of the current to the incident optical power, the responsivity (R_λ) can be calculated using the equation $R_\lambda = (I_\lambda - I_d)/P_\lambda S$, where I_λ is the photocurrent, I_d is the dark current, P_λ is the light intensity, and S is the effective illuminated area.[28] Because the photocurrent is much larger than the dark current ($I_\lambda - I_d \approx I_\lambda$), the responsivity depends linearly on the photocurrent. The responsivity of the 254 nm light presents an exponential increase with increasing voltage from 0 V to −6 V, as shown in Supporting Information Figure S4a, and a linear increase from the voltage higher than −6 V for the resistance-restricted effect in a high photocurrent. In addition, the responsivity under −10 V at 254 nm is 5.18×10^3 A/W, which is the largest value obtained with the Ga$_2$O$_3$ photodetector.[45]

The external quantum efficiency (EQE) of the fabricated photodetector could be calculated from the measured spectral response with the equation $\eta = R_\lambda hc/q\lambda$, where η is the EQE, R_λ is the measured responsivity, e is the electron charge, λ is the incident light wavelength, h is the Planck constant, and c is the speed of light.[28] It is found that the EQE is directly proportional to the responsivity and can be as high as $2.53 \times 10^6\%$ under −10 V bias. The large EQE of the device implies that there is a high internal gain in our photodetector. As shown in the inset of Figure 3b, under the reverse bias, the dark current maintains an approximately linear increase ($\sim 10^{-11}$ A) from 0.1 to 4.3 V, but increases exponentially (10^{-10} A to 10^{-7} A) from 4.3 to 10 V, which implies that the device has a

breakdown voltage of 4.3 V at room temperature. There are two nondestructive breakdown mechanisms for a diode: Zener tunneling and avalanche multiplication. The Zener tunneling mechanism usually has a negative temperature coefficient, and the avalanche multiplication has a positive temperature coefficient.[40] Figure 3c shows the reverse current under different temperatures, from which we can clearly observe the increasing breakdown voltage (from 4.3 to 6.4 V) with the increase in temperature from 300 to 370 K. A positive temperature coefficient of 0.03 V/K was obtained for this device. These results suggest that our device is an avalanche photodiode and that avalanche multiplication dominates the internal gain in our photodetector. The avalanche gain (M) of the structure can be determined using $M = (I_{ph} - I_d)/(I_{ph0} - I_{d0})$, where I_{ph} and I_d are the multiplied photocurrent and dark current, respectively, and I_{ph0} and I_{d0} are the unmultiplied photocurrent and dark current, respectively.[40] Because the photocurrent of the photodiode does not significantly increase above 0.3 V, the unmultiplied current is sampled at 0.3 V for calculating the avalanche gain. The extracted avalanche gain of the APD device could reach a maximum value of 2.92×10^4 under the reverse bias of 10 V, which is large than the value of AlGaN APDs (1560).[16]

The linear dynamic range (LDR, typically quoted in dB) is one of the important figure-of-merits for a photodetector and can be obtained from the equation LDR = 20log (I^*_{ph}/I_{dark}), where I^*_{ph} is the photocurrent, measured at light intensity of 1.67 mW/cm^2.[36,46] As shown in Supporting Information Figure S4b, the LDR value increases to the highest value of 119.3 dB at −5 V, and then decreases as the voltage increases in the reverse bias. The calculated LDR is equal to those of Si photodetectors (120 dB) and is larger than those of InGaAs photodetectors (66 dB).[46] The high LDR indicates a relatively large ratio of photocurrent to dark current and a high signal-to-noise ratio. The detectivity (D^*) is one of the key figure-of-merits for a photodetector, which usually describes the smallest detectable signal.[36] For solar blind photodetectors that are based on wide band gap semiconductors, the noise current caused by background radiation is far less than that from thermal energy and the shot noise from dark current. Because of the large resistance and low driven voltage, the thermal-related noise has little effect on the device noise. In this case, the shot noise is the major contributor to the total noise; therefore, the detectivity of a photodetector can be determined by $D^* = R_\lambda/(2qJ_d)^{1/2}$, where R is the responsivity of the photodector, q is the elemental charge, and J_d is the dark current density.[47] As shown in Supporting Information Figure S4c, the D^* value increases to the highest value of 9.91×10^{14} cm·Hz$^{1/2}$/W (Jones) at −6 V and then decreases as the voltage increases in the reverse bias. The detectivity is a parameter that can comprehensively evaluate the responsivity and dark current. A responsivity of 1.3×10^3 A/W and a dark current of 5.35×10^{-10} A at −6 V bias suggests the detectivity get the maximum value. All of the following tests, therefore, are measured at −6 V bias.

The spectral response of the APD device at −6 V bias could be directly measured as shown in Figure 4a. The peak photoresponse is located at 254 nm, which corresponds to the band gap of Ga$_2$O$_3$ (4.9 eV), and there is no obvious photoresponse peak ($\sim$370 nm) corresponding to the band gap of ZnO (3.37 eV). The responsivity curve has a sharp cutoff wavelength at 266 nm (<280 nm), as shown in the inset of Figure 4a, which indicates that this device is indeed a solar-blind photodetector. In addition, the UV/visible rejection ratio
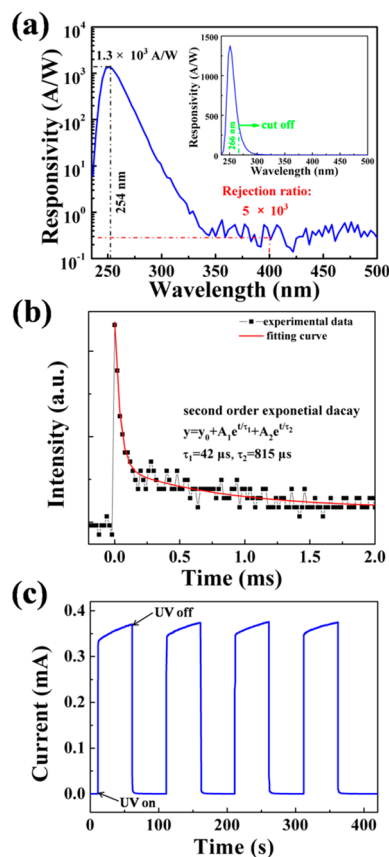
Figure 4. (a) Spectral response of the device at −6 V bias. (b) Pulse response of the device at −6 V bias and a second-order exponential fit of the data. (c) Time-resolved photocurrent with the UV light (254 nm, 1.67 mW/cm^2) on and off for four cycles at −6 V bias.

(R_{254nm}/R_{400nm}) is approximately 5×10^3, which implies that the photodetector has a relatively high spectral selectivity to solar-blind UV. The response time of the APD device at −6 V has been measured as shown in Figure 4a. From the experimental data, we can calculate that the rise time of the APD at −6 V is less than 20 μs, which is the interval time between two points. The decay time could be well fitted using a second-order exponential formula.[48] The best fitting at −6 V yields $\tau_1 = 42$ μs and $\tau_2 = 815$ μs, which are the shortest decay time for a Ga$_2$O$_3$ photodetector. To evaluate the combination property of the APD, the time-resolved photocurrent of the device has been measured under illumination by 254 nm UV light with 1.67 mW/cm^2. The light is repeatedly turned on and off with a working voltage of −6 V, as shown in Figure 4c. The device shows a large and fast response to the weak 254 nm light, and the dynamic response demonstrates that the device is stable and that its performance is reproducible in practical applications. The performance parameters of the ZnO−Ga$_2$O$_3$ core−shell structure solar-blind photodetector are compared with that of β-Ga$_2$O$_3$ nanostructures photodetectors, an Al$_x$Ga$_{1-x}$N APD, and a commercial Si APD optical device in Supporting Information Table S1. As shown in Supporting Information Table S1, the response speed of this APD device are much faster than that of the photoconductivity photo-detectors based on β-Ga$_2$O$_3$ nanostructures; the responsivity and detectivity of this APD device are much larger than that of the commercial Si APD device. These results all show that the

ZnO−Ga$_2$O$_3$ core−shell structure device is highly suitable for solar-blind UV detection.

We propose the following analysis of the mechanism of avalanche breakdown. From Figure 3b, we can see that the resistance under the forward bias is approximately 10^4 Ω and that the resistance under the reverse bias is approximately 10^{10} Ω, which means that the current is dominated by the junction. Both ZnO and Ga$_2$O$_3$ are n-type semiconductors, which suggests that the contact between them forms an n−n heterojunction and electrons dominate the conductivity of the device. To better understand the APD formation mechanism of the ZnO−Ga$_2$O$_3$ core−shell structure, the energy band diagram is shown in Figure 5a. In this diagram,
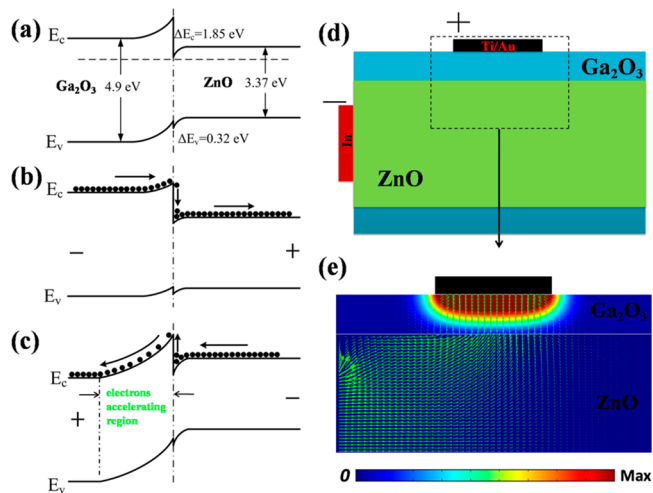
Figure 5. Energy band diagram of the APDs device (a) with no bias, (b) in forward bias, (c) in reverse bias. (d) The sectional view of schematic diagram of the device. (e) Simulated electric potential distribution and electron tracking of the device.

the electron affinities (χ) of Ga$_2$O$_3$ and ZnO are taken as 2.5 and 4.35 eV, respectively, and the band gaps of Ga$_2$O$_3$ and ZnO are 4.9 and 3.37 eV, respectively.[38] The energetic barrier for electrons (ΔE_c) and holes (ΔE_v) are 1.85 and 0.32 eV, respectively. The ΔE_c between ZnO and Ga$_2$O$_3$ is much larger than the ΔE_v, which could lead to the impact ionization of the electrons generating an avalanche multiplication effect.[40] When the device is under a forward bias, the electrons move from Ga$_2$O$_3$ to ZnO, which is shown as the energy band diagram in Figure 5b. As the energy band of Ga$_2$O$_3$ is enhanced and the energy band of ZnO is reduced, the barrier region at the interface is lower, which facilitates electron transfers from Ga$_2$O$_3$ to ZnO. Under a reverse bias, the electrons move from ZnO to Ga$_2$O$_3$, which is shown as the energy band diagram in Figure 5c. Because the high ΔE_c can efficiently block the injection of electrons from ZnO to Ga$_2$O$_3$, the circuit presents a cutoff state. When the electrons overcome the high ΔE_c, they enter the space charge region that can act as an electron-accelerating region.[49] Upon the increasing the reverse bias, the electron-accelerating region is broadened. The avalanche multiplication is affected by the impact ionization of the electrons, which strongly depends on the applied electric field.[50−52] The electric potential distribution of the device is shown in Figure 5e. When a reverse bias voltage is applied on the device, the potential drop mainly occurs in the region of the Ga$_2$O$_3$ shell under the Ti/Au electrode. Considering that the thickness of the shell is approximately 500 nm, the applied

voltage of −10 V leads to an electric field reaching 200 kV/cm. Under such a high electric field, the electrons will gain much kinetic energy and impact Ga_2O_3 lattice to induce the avalanche breakdown.[50,51] As shown in Figure 3b, this device is a typical diode, and presents an off state in the reverse bias and an on state in the forward bias. When it is in the reverse bias, the dark current is very low, and the photoinduced carriers are involved in an avalanche multiplication process; therefore, the photocurrent is much larger than the dark current. When it is in the forward bias, the circuit is in an open state, and the current under illumination is much less than the darkcurrent; therefore, the photocurrent appears almost unchanged compared with the dark current. As shown in Figure 5c, the ZnO side is an electrons accumulation region and the Ga_2O_3 side is the electrons depletion region. Hence, the circuit is controlled by the Ga_2O_3 side: the photoinduced by the ZnO region is still difficult overcome by the high ΔE_c, which will not result in the increase of photocurrent, whereas the photoinduced by the Ga_2O_3 region can easily move toward to the electrodes, which will result in the increase of photocurrent. And this is consistent with the spectral response of device in Figure 4a.

In summary, $ZnO–Ga_2O_3$ core–shell microwires with high crystal quality have been synthesized by a simple one-step method. A solar-blind APD has been fabricated based on this $ZnO–Ga_2O_3$ core–shell microwire, which showd a high performance in terms of a high responsivity (1.3×10^3 A/W), a high detectivity (9.91×10^{14} cm·Hz$^{1/2}$/W), and a fast response time (20 μs) under −6 V bias. The key photoresponse performances of this APD in the solar-blind waveband can compete with that of commercial Si APD (APD120A2 in Thorlabs company) with responsivity ∼8 A/W, detectivity ∼10^{12} cm·Hz$^{1/2}$/W, response time ∼20 ns. A positive temperature coefficient confirmed that the high internal gain of our photodiode originates from the avalanche multiplication. All of the device parameters implied that this $ZnO–Ga_2O_3$ core–shell microwire APD is highly suitable for practical applications of solar-blind photodetection. Moreover, this core–shell microstructure heterojunction design method would provide a new approach to realize the APD device.

■ ASSOCIATED CONTENT

ⓈSupporting Information

Details for preparation and characterizations of samples, and additional figures. The Supporting Information is available free of charge on the ACS Publications website at DOI: 10.1021/acs.nanolett.5b00906.

■ AUTHOR INFORMATION

Corresponding Authors

*E-mail: xshfang@fudan.edu.cn.
*E-mail: zhaodx@ciomp.ac.cn.

Notes

The authors declare no competing financial interest.

■ ACKNOWLEDGMENTS

■ REFERENCES

(1) Razeghi, M.; Rogalski, A. J. Appl. Phys. **1996**, 79, 7433−7473.

(2) Razeghi, M. Proc. IEEE **2002**, 90, 1006−1014.

(3) Monroy, E.; Omnes, F.; Calle, F. Semicond. Sci. Technol. **2003**, 18, 33−51.

(4) Omnes, F.; Monroy, E.; Munoz, E.; Reverchon, J. L. Proc. SPIE **2007**, 6473, 1−15.

(5) Oshima, T.; Okuno, T.; Arai, N.; Suzuki, N.; Hino, H.; Fujita, S. Jpn. J. Appl. Phys. **2009**, 48, 011605.

(6) Xu, Z. Y.; Sadler, B. M. IEEE Commun. Mag. **2008**, 46, 67−73.

(7) Chen, G.; Xu, Z. Y.; Ding, H. P.; Sadler, B. M. Opt. Express **2009**, 17, 3929−3940.

(8) Soci, C.; Zhang, A.; Xiang, B.; Dayeh, S. A.; Aplin, D. P. R.; Park, J.; Bao, X. Y.; Lo, Y. H.; Wang, D. Nano Lett. **2007**, 7, 1003−1009.

(9) Jin, Y.; Wang, J.; Sun, B.; Blakesley, J. C.; Greenham, N. C. Nano Lett. **2008**, 8, 1649−1653.

(10) Bulgarini, G.; Reimer, M. E.; Hocevar, M.; Bakkers, E. P. A. M.; Kouwenhoven, L. P.; Zwiller, V. Nat. Photonics **2012**, 6, 455−458.

(11) Kardynal, B. E.; Yuan, Z. L.; Shields, A. J. Nat. Photonics **2008**, 2, 425−428.

(12) Liao, M. Y.; Sang, L. W.; Teraji, T.; Imura, M.; Alvarez, J.; Koide, Y. Jpn. J. Appl. Phys. **2012**, 51, 090115.

(13) Thomas, O.; Yuan, Z. L.; Shields, A. J. Nat. Commun. **2012**, 3, 644.

(14) Wood, R. W. Phys. Rev. **1933**, 44, 353−360.

(15) Clarke, J. T.; Skinner, W. R.; Vincent, M. B.; Irgang, T.; Suratkal, V.; Grassl, H.; Trauger, J. T. Appl. Opt. **1999**, 38, 1803−1813.

(16) Tut, T.; Gokkavas, M.; Inal, A.; Ozaby, E. Appl. Phys. Lett. **2007**, 90, 163506.

(17) Tut, T.; Yelboga, T.; Ulker, E.; Ozbay, E. Appl. Phys. Lett. **2008**, 92, 103502.

(18) Sang, L.; Liao, M.; Sumiya, M. Sensors **2013**, 13, 10482−10518.

(19) Konstantatos, G.; Sargent, E. H. Nat. Nanotechnol. **2010**, 5, 391−400.

(20) Li, Y.; Tokizono, T.; Liao, M.; Zhong, M.; Koide, Y.; Yamada, I.; Delaunay, J. J. Adv. Funct. Mater. **2010**, 20, 3972−3978.

(21) Li, L.; Auer, E.; Liao, M. Y.; Fang, X. S.; Zhai, T. Y.; Gautam, U. K.; Lugstein, A.; Koide, Y.; Bando, Y.; Golberg, D. Nanoscale **2011**, 3, 1120−1126.

(22) Feng, W.; Wang, X.; Zhang, J.; Wang, L.; Zheng, W.; Hu, P.; Cao, W.; Yang, B. J. Mater. Chem. C **2014**, 2, 3254−3259.

(23) Hatch, S. M.; Briscoe, J.; Dunn, S. Adv. Mater. **2013**, 25, 867−871.

(24) Luo, L. B.; Chen, J. J.; Wang, M. Z.; Hu, H.; Wu, C. Y.; Li, Q.; Wang, L.; Huang, J. A.; Liang, F. X. Adv. Funct. Mater. **2014**, 24, 2794−2800.

(25) Hong, Q.; Cao, Y.; Xu, J.; Lu, H.; He, J.; Sun, J. L. ACS Appl. Mater. Interfaces **2014**, 6, 20887−20894.

(26) Hsu, C. L.; Lu, Y. C. Nanoscale **2012**, 4, 5710−5717.

(27) Nakagomi, S.; Momo, T.; Takahashi, S.; Kokubun, Y. Appl. Phys. Lett. **2013**, 103, 072105.

(28) Weng, W. Y.; Hsueh, T. J.; Chang, S. J.; Huang, G. J.; Hsueh, H. T. IEEE Sensors J. **2011**, 11, 999−1003.

(29) Lauhon, L. J.; Gudiksen, M. S.; Wang, D.; Lieber, C. M. Nature **2002**, 420, 57−61.

(30) Tian, B. Z.; Zheng, X. L.; Kempa, T. J.; Fang, Y.; Yu, N. F.; Yu, G. H.; Huang, J. L.; Lieber, C. M. Nature **2007**, 449, 885−890.

(31) Tang, J.; Huo, Z.; Brittman, S.; Gao, H.; Yang, P. Nat. Nanotechnol. **2011**, 6, 568−572.

(32) Hu, L. F.; Brewster, M. M.; Xu, X. J.; Tang, C. C.; Gradecak, S.; Fang, X. S. Nano Lett. **2013**, 13, 1941−1947.

(33) Dai, X.; Zhang, S.; Wang, Z.; Adamo, G.; Liu, H.; Huang, Y.; Couteau, C.; Soci, C. Nano Lett. **2014**, 14, 2688−2693.

(34) Smith, A. M.; Lane, L. A.; Nie, S. Nat. Commun. **2014**, 5, 4506.

(35) Mazeina, L.; Picard, Y. N.; Prokes, S. M. Cryst. Growth Des. **2009**, 9, 1164−1169.

(36) Liu, X.; Gu, L.; Zhang, Q.; Wu, J.; Long, Y.; Fan, Z. Nat. Commun. **2014**, 5, 4007.

(37) Afsal, M.; Wang, C. Y.; Chu, L. W.; Ouyang, H.; Chen, L. J. *J. Mater. Chem.* **2012**, *22*, 8420−8425.

(38) Zhang, L.; Li, Q.; Shang, L.; Zhang, Z.; Huang, R.; Zhao, F. *J. Phys. D: Appl. Phys.* **2012**, *45*, 486103.

(39) Yang, K.; East, J. R.; Haddad, G. I. *Solid St. Electron.* **1993**, *36*, 321−330.

(40) Sze, S. M.; Ng, K. K. *Physics of Semiconductor Devices*, 3rd ed.; Wiley: Hoboken, NJ, 2007.

(41) Chang, K. W.; Wu, J. J. *J. Phys. Chem. B* **2005**, *109*, 13572−13577.

(42) Huang, Y.; Zhang, Y.; He, J.; Dai, Y.; Gu, Y.; Ji, Z.; Zhou, C. *Ceram. Int.* **2006**, *32*, 561−566.

(43) Fang, F.; Zhao, D. X.; Li, B. H.; Zhang, Z. Z.; Zhang, J. Y.; Shen, D. Z. *Appl. Phys. Lett.* **2008**, *93*, 233115.

(44) Chang, M. P.; Chiang, M. H.; Lin, W. T.; Lee, C. T. *Mater. Lett.* **2011**, *65*, 1473−1475.

(45) Zou, R.; Zhang, Z.; Liu, Q.; Hu, J.; Sang, L.; Liao, M.; Zhang, W. *Small* **2014**, *10*, 1848−1856.

(46) Liu, S.; Wei, Z. M.; Cao, Y.; Gan, L.; Wang, Z. X.; Xu, W.; Guo, X. F.; Zhu, D. B. *Chem. Sci.* **2011**, *2*, 796−802.

(47) Gong, X.; Tong, M.; Xia, Y.; Cai, W.; Moon, J. S.; Cao, Y.; Yu, G.; Shieh, C.; Nilsson, B.; Heeger, A. J. *Science* **2009**, *325*, 1665−1667.

(48) Ni, P. N.; Shan, C. X.; Wang, S. P.; Liu, X. Y.; Shen, D. Z. *J. Mater. Chem. C* **2013**, *1*, 4445−4449.

(49) Wei, W.; Xu, G.; Wang, T.; Shen, W. Z. *Thin Solid Films* **2007**, *515*, 3997−4002.

(50) Chen, T. P.; Chen, W. H.; Lee, C. J.; Chu, K. Y.; Chen, L. Y.; Hung, C. W.; Tsai, T. H.; Cheng, S. Y.; Liu, W. C. *J. Appl. Phys.* **2008**, *103*, 114506.

(51) Rothman, J.; Mollard, L.; Bosson, S.; Vojetta, G.; Foubert, K.; Gatti, S.; Bonnouvrier, G.; Salveti, F.; Kerlain, A.; Pacaud, O. *J. Electron. Mater.* **2012**, *41*, 2928−2936.

(52) Wang, X.; Hu, W.; Pan, M.; Hou, L.; Xie, W.; Xu, J.; L, X.; Chen, X.; Lu, W. *J. Appl. Phys.* **2014**, *115*, 013103.